RAM ROBOTICS AND MECHATRONICS

# IMPLEMENTATION AND EVALUATION OF A MULTI-AXIS BRUSHLESS DC MOTOR CONTROL USING A PLANAR FINITE ELEMENT APPROACH

B. (Bram) Eijking

MSC ASSIGNMENT

**Committee:**
prof. dr. ir. L. Abelmann
dr. V. Groenhuis, MSc
dr. F.J. Siepel, MSc
dr. ir. W.B.J. Hakvoort

February, 2021

011RaM2021
Robotics and Mechatronics
EEMCS
University of Twente
P.O. Box 217
7500 AE Enschede
The Netherlands

UNIVERSITY OF TWENTE. | TECHMED CENTRE
UNIVERSITY OF TWENTE. | DIGITAL SOCIETY INSTITUTE

# Contents

## Abstract

In certain applications it is desirable to have compact solutions that are able to drive multiple degrees of freedom. This could be realized by means of a multi-motor design that features concentric axes that can be independently driven. This report will show a first step towards testing and validation of a Brushless Direct Current (BLDC) multi-motor and two control methods will be tested and validated using a planar finite element method. This planar finite element method was first validated using simplified models that can also be approximated analytically such that the results can be compared and the accuracy can be determined. A prototype was built with two ouput shafts on which measurements were conducted which were compared to the results obtained through the Finite Element Method Magnetics (FEMM) model. Based on the obtained results it was shown that it is possible to achieve the required output torque on both output shafts such that the outputs can be decoupled using a controller. Besides this analysis a comparison was made between two different control techniques being sinusoidal and trapezoidal control. From the results it was shown that sinusoidal control has a benefit in the fact that the torque ripple is reduced significantly as well as reducing the cross link torque for one of the outputs significantly.

# 1 Introduction

In this report a new type of BLDC motor will be tested, which features multiple output shafts and a shared stator. This will be done through Finite element simulations and a prototype will be built. With this approach we will answer the following research question:

How accurately can different control methods be validated and tested using a planar finite element model for BLDC multimotors?

In order to answer this research question the first step that will be discussed in the method will be to validate the finite element program that was used for this project. This will be done by analyzing three different model that can also be computed analytically such that the results can be compared and possible limitations can be found. The first model will be using the dipole model for a permanent magnet to compute the flux density far away from the magnet. This model will be derived for a planar field only which can be done by taking an infinitely long magnet. Secondly two models with different sources of magnetic flux and a core made of soft magnetic material will be discussed. The first model contains a permanent magnet and the second model contains a coil. These models will be used to compute the flux density inside a small air gap. With these three models the parts of a BLDC motor that contribute to the magnetic fields are validated.
After the finite element method was validated a prototype will be shown on which measurements are performed. These measurements will be compared to the finite element analysis to show if the model matches the real implementation of the motor.
Lastly two control methods will be validated using the finite element approach. The prototype suffered from some inaccuracies in the design of this motor which made it impossible to do extensive measurements on this motor, therefore the control methods will only be tested using the finite element model. The two control methods that will be compared are trapezoidal control and sinusoidal control. The latter is commonly called field oriented control. The goal is to show that using these control methods we can obtain a functional multimotor by showing that the two outputs are independent of each other and that the cross linkage between input wave forms and outputs is smaller when compared to the nominal output torque.

# 2 Background

BLDC motors have the advantage of generating high power output relative to the motors size and require low maintenance compared to brushed motors. In this project a multi degree of freedom (DOF) motor will be designed and tested with a new concentric design that features multiple rotors that are driven by a single set of coils which distinguishes it from previous research. Previous research and ongoing research into multi DOF BLDC motors include dual rotor/stator designs, 3 DOF spherical motor designs, dual rotor single stator designs and dual stator single rotor designs.

## 2.1 Dual rotor and stator motor

The first design to be discussed consists of a motor with a dual stator and dual rotor design. In this design the two rotors are a combination of an inrunner and outrunner rotor. The stator core is placed in between the two rotors and feature two separate windings. This way the two rotors can be seen as separate motors and can be individually driven. A conceptual design of this is shown in figure 1a.

The advantage of such a design is the simplicity of controlling the two separate rotors since they can be controlled similarly as two separate motors. The disadvantages are that it is limited to two degrees of freedom and that it requires two separate sets of windings and two separate controllers to control the two DOFs.

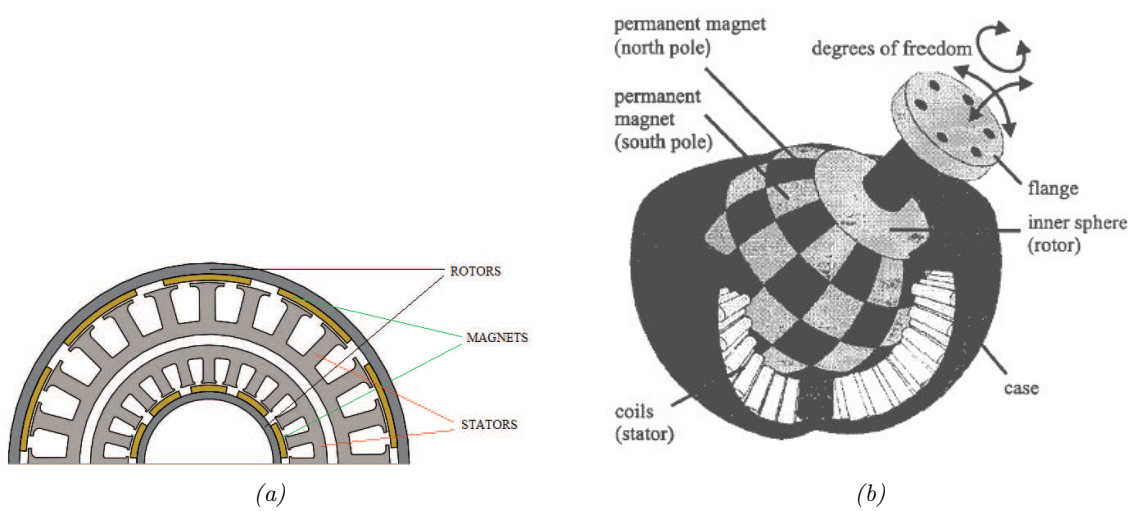


*(a)* *(b)*

Figure 1: (a) Conceptual design of a dual rotor, dual stator motor [1]. (b) Spherical motor design with 3 degrees of freedom [2].

## 2.2 Spherical motor with three degrees of freedom

The second design to be discussed is a motor which has three perpendicular rotational DOFs [2], [3]. This spherical design can be used as an actuated joint and pointing the main axis of the motor as well as rotate the main axis of the motor. A conceptual design of this motor type is shown in figure 1b.

The main advantage of this design is that it provides multiple degrees of freedom that can be used as an actuated joint in a compact design. The disadvantage is that it is complex to produce such a motor as well as a complex controller is needed to control the degrees of freedom.

## 2.3 Dual rotor single stator motor

The third design to be discussed features a dual rotor and single stator design [4]. This design is similar to the design that was proposed for this project in the fact that it features a single set of windings and a single stator core that is used to control multiple degrees of freedom. The two rotors are distinguished by having a different number of magnet poles. In this design it was chosen to apply an axial magnetic field in the rotor. This motor is limited to two degrees of freedom if used with a single stator. A conceptual design is shown in figure 2a.

## 2.4 Dual stator single rotor motor

The last design that will be discussed here is a motor with a single rotor and dual stator design [5]. This motor has one linear DOF and a rotational DOF. The magnets and windings are placed orthogonal to obtain the two degrees of freedom such that the motor can move linearly along the shaft as well as rotate. This motor is also limited to two DOFs, however the combination of both linear as well as rotation is unique. A conteptual design is shown in figure 2b.

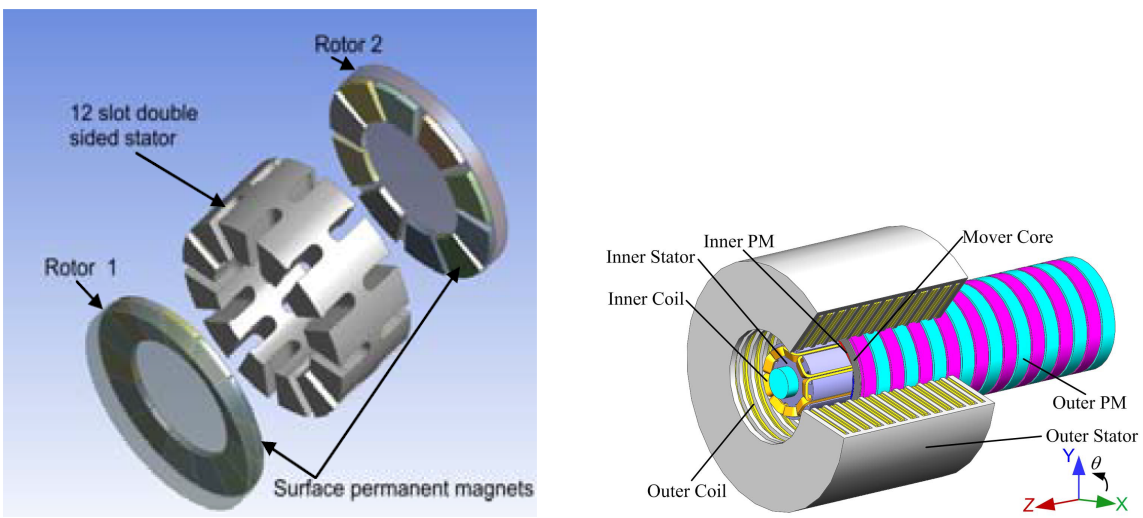


*(a)* *(b)*

Figure 2: (a) Design of a motor with a dual rotor and single stator [4]. (b) Design of a rotary-linear motor [5].

As can be seen above there are several different configurations possible to achieve a multimotor. There are different possibilities for the driving technique as well as the way in which the output degrees of freedom of the motor are configured has many different possibilities. The multimotor that will be implemented and tested in this report distinguishes itself from the previously shown examples from the literature. The main difference is in the way the output shafts are placed as they are mounted concentrically to each other. This shaft assembly will then have multiple rotors mounted to it and it will be placed in a common radially mounted stator. This way the coils are shared between all rotors. This way multiple shafts can be a added to the motor and potentially even more degrees of freedom can be achieved compared to the examples shown above. A more detailed description of this motor design will be discussed in the method section.

# 3 Method

To verify the FEMM model first three analytical models will be discussed and compared to FEMM simulations. These simplified models were chosen such that they can be computed analytically. After that the prototype for the multimotor with two output shafts that was built will be shown as well as the FEMM model that was made to perform calculations on this motor. The measurement setup that was used to measure static torque on this motor will be shown and lastly the two control methods that were analyzed will discussed.

## 3.1 Dipole model:

To model the motor torque the program FEMM is used, this is a 2D finite element method in which the field and torque can be computed. To verify that the finite element method shows good results the first step that was taken was to make several simplified models that can be solved analytically of which the results are compared to the finite element results. The first model that will be tested is a dipole model. For this a small permanent magnet is used and the field at a distance is measured. The dipole field representation in vector notation is as follows [6]:

$$\boldsymbol{B}_{\text{dip}}(\mathbf{r}) = \frac{\mu_0}{4\pi}\frac{1}{r^3}\left[3(\mathbf{m}\cdot\hat{\mathbf{r}})\hat{\mathbf{r}} - \mathbf{m}\right] \tag{1}$$

In this equation the magnetic moment is represented by $\mathbf{m}$, vector $\mathbf{r}$ is pointing from the dipole to the point at which the field is measured. The field measured at points in the direction of the magnetic moment can be simplified since the inner product of the unit vector $\hat{\mathbf{r}}$ multiplied by that unit vector is equal to the magnetic moment itself therefore at any $\mathbf{r}$ parallel to $\mathbf{m}$ the field becomes:

$$\mathbf{B}_{\text{dip}}(\mathbf{r}) = \frac{\mu_0}{4\pi r^3}\left[3\mathbf{m} - \mathbf{m}\right] \tag{2}$$

$$\boldsymbol{B}_{\text{dip}}(\mathbf{r}) = \frac{\mu_0}{2\pi r^3}\cdot\mathbf{m} \tag{3}$$

When taking the vector $\mathbf{r}$ orthogonal to the magnetic moment the field can be simplified since the inner product of orthogonal vectors is zero. This yields the following relation for the dipole field when $\mathbf{r}$ is orthogonal to the magnetic moment:

$$\mathbf{B}_{\text{dip}}(\mathbf{r}) = \frac{\mu_0}{4\pi r^3}\left[3\cdot\mathbf{0} - \mathbf{m}\right] \tag{4}$$

$$\mathbf{B}_{\text{dip}}(\mathbf{r}) = -\frac{\mu_0}{4\pi r^3}\cdot\mathbf{m} \tag{5}$$

To compare this dipole model to the FEMM results a permanent magnet will be used. When the distance from the magnet is large enough the field created by a magnet can be approximated by a dipole field with magnetic moment:

$$\mathbf{m} = \frac{1}{\mu_0}\mathbf{B}_{\text{r}}\cdot V \tag{6}$$

With permeability of free space $\mu_0$, residual flux density of the magnet and the volume of the magnet. Substituting this magnetic moment into the two dipole equations 3 and 5 gives the following field description for the dipole model:

$$\mathbf{B}_{\text{dip}}(r_x) = \frac{\mathbf{B}_r\cdot V}{2\pi r_x^3} \tag{7}$$

$$\mathbf{B}_{\text{dip}}(r_y) = \frac{\mathbf{B}_r\cdot V}{4\pi r_y^3} \tag{8}$$

When comparing this result in FEMM a large error was observed which increases linearly in $r$. This can be explained by the fact that FEMM only models the planar fields. To validate this an approximation is made using an infinitely long bar magnet. This ensures that the field will not have any components in the z-direction and therefore it should match well with the planar model. The magnetic moment of a permanent magnet can be modelled as a surface current that is perpendicular to the magnetic moment resulting in a coil of which the field is identical to that of the permanent magnet. Applying this to the permanent magnet results in two infinitely long wires carrying a current $I$ with the same dimensions as the permanent magnet. The magnet has width and height $d$ and length $L$, in order to find the field the combined field of the two infinitely long wires will be added as follows:

$$\mathbf{B}_{\text{total}}(r) = \mathbf{B}_1(r) + \mathbf{B}_2(r-d) \tag{9}$$

The field of a single infinitely long wire is described as shown in equation 10 for which the surface current for a permanent magnet is defined by the residual magnetic flux density [7] [8]. The magnetic moment can be computed as shown in equation 11 which can then be substituted with the magnetic moment of the permanent magnet as discussed previously. This model is derived in cylindrical coordinates.

$$\mathbf{B} = \frac{\mu_0}{2\pi}\frac{I}{r} \cdot \hat{\boldsymbol{\phi}} \tag{10}$$

$$\mathbf{m} = IA\hat{\boldsymbol{\phi}} = ILd\hat{\boldsymbol{\phi}} \tag{11}$$

Substituting this into the total field equation gives the following from which the field as a function of the distance $\mathbf{r}$ can be determined. For this equation $\mathbf{r}$ is taken as a vector perpendicular to the magnetic moment such that the offset from the origin only results in a difference in the length of the $\mathbf{r}$ vector. This difference in length is equal to the width of the permanent magnet $d$.

$$\mathbf{B}_{\text{total}} = \frac{\mu_0}{2\pi}\frac{I}{r} \cdot \hat{\boldsymbol{\phi}} - \frac{\mu_0}{2\pi}\frac{I}{r-d} \cdot \hat{\boldsymbol{\phi}} \tag{12}$$

$$\mathbf{B}_{\text{total}} = -\frac{\mu_0 I d}{2\pi(r^2 - rd)} \cdot \hat{\boldsymbol{\phi}} \tag{13}$$

Since we are interested in the far field of the permanent magnet the term in the denominator can be approximated by only taking the $\mathbf{r}^2$ terms and the magnetic moment $\mathbf{m}$ is substituted for the current model.

$$\mathbf{B}_{\text{total}} = -\frac{\mu_0 I d}{2\pi r^2} \cdot \hat{\boldsymbol{\phi}} \tag{14}$$

$$\mathbf{B}_{\text{total}} = -\frac{\mu_0}{2\pi r^2 L}\mathbf{m} \tag{15}$$

Now the magnetic moment for a permanent magnet can be substituted which depends on its residual flux density and the volume of the magnet. Doing so yields the final representation for the magnetic field of the bar magnet:

$$\mathbf{B}_{\text{total}} = -\frac{d^2}{2\pi r^2} \cdot \mathbf{B}_r \tag{16}$$

### 3.2 Yoke model with permanent magnet:

The second model that will be used for validating the FEMM results is an analytical model to describe the flux density inside the air gap of a yoke in combination with a permanent magnet. The geometry that will be discussed is shown in figure 3a. This model can be seen as a series magnetic circuit with a yoke that

is made of a material with infinite magnetic permeability, this way we can evaluate the influence of the permanent and the air gap. To determine the flux density inside the air gap a lumped element model is used where the magnetic circuit is modelled as an equivalent circuit. First the permanent magnet will be considered, the magnetic flux density of a permanent magnet is described by the BH curve which describes the flux density at different field strengths. This curve is described as follows [9]:

$$B_{\mathrm{m}} = B_{\mathrm{r}} - \mu_0 \mu_{\mathrm{r}} \cdot H \tag{17}$$

With residual flux density $B_{\mathrm{r}}$, permeability of air $\mu_0$, magnet relative permeability $\mu_{\mathrm{r}}$. The magnetomotive force $F_{\mathrm{m}}$ and flux $\phi_{\mathrm{m}}$ in the magnet can be determined based on the magnet thickness $h_{\mathrm{m}}$ and surface area $S_{\mathrm{m}}$ as follows:

$$F_{\mathrm{m}} = H \cdot h_{\mathrm{m}} \tag{18}$$

$$\phi_{\mathrm{m}} = B_{\mathrm{m}} \cdot S_{\mathrm{m}} \tag{19}$$

Using this equation the flux inside the magnet can be related to the flux density and magnetomotive force by substituting equation 17 with the flux and magnetomotive force.

$$\phi_{\mathrm{m}} = B_{\mathrm{r}} \cdot S_{\mathrm{m}} - \mu_0 \mu_{\mathrm{r}} H \cdot S_{\mathrm{m}} = B_{\mathrm{r}} \cdot S_{\mathrm{m}} - \frac{\mu_0 \mu_{\mathrm{r}} S_{\mathrm{m}}}{h_{\mathrm{m}}} \cdot F_{\mathrm{m}} \tag{20}$$

From this equation the permanent magnet can be seen as a combination of a flux source with an internal reluctance. Combining this with the remaining parts of the magnetic circuit gives an equivalent circuit. This equivalent circuit can also be directly computed using Ampere's law, which states that the magnetic field around a closed loop integral is equal to the total current passing through the loop which is zero in the case of a permanent magnet. Using this approach gives the following [10]:

$$\oint_C H d\ell = \int_S J \cdot dS = 0 \tag{21}$$

In this model the permeability of the core material is assumed to have infinite permeability therefor no reluctance, which results in a field equal to zero. This means the field that is left is the field inside the magnet and the field inside the air gap. As shown above we can determine the field inside the magnet from the BH curve. Applying Ampere's law to the model gives the following:

$$H_g g + H_{\mathrm{m}} h_{\mathrm{m}} = 0 \tag{22}$$

$$H_{\mathrm{m}} = -\frac{g}{h_{\mathrm{m}}} H_g \tag{23}$$

With the field inside the air gap $H_g$ and gap length $g$. Now assuming the flux is contained inside the magnetic circuit the flux through the air gap is equal to the flux through the magnet with an equal surface area therefor an equal flux density. Using this assumption we can relate the air gap flux density to the properties of the permanent by using the relation between the flux density and magnetic field shown in equation 17 and the relation between the magnetic field in the air gap and the magnet described above.

$$\mu_0 H_g = \mu_0 \mu_{\mathrm{r}} H_{\mathrm{m}} + B_{\mathrm{r}} = -\mu_0 \mu_{\mathrm{r}} \frac{g}{h_{\mathrm{m}}} H_g + B_{\mathrm{r}} \tag{24}$$

$$B_g = \mu_0 H_g = \frac{h_{\mathrm{m}}}{h_{\mathrm{m}} + \mu_{\mathrm{r}} g} \cdot B_{\mathrm{r}} \tag{25}$$

This equation can be interpreted based on the equivalent circuit approach as it shows the flux density in a parallel reluctance, since the reluctance's for the permanent magnet and air gap are dependent on their height. This analytical model will be used to compare to the FEMM model as shown in figure 3a.

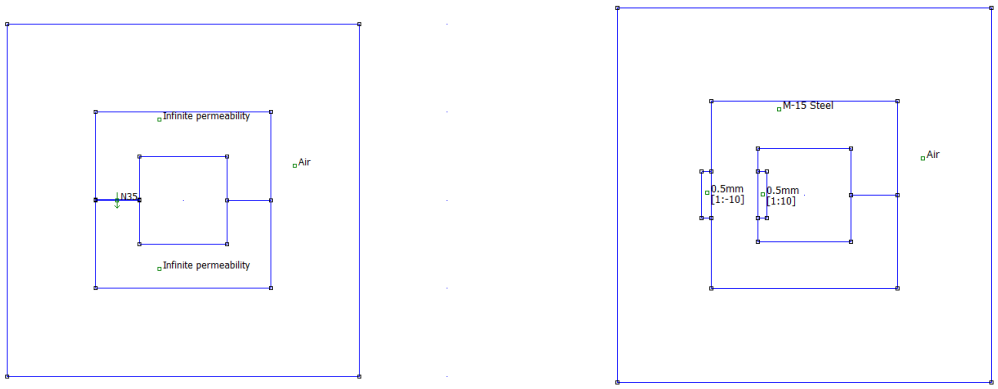


*(a)* *(b)*

Figure 3: (a) FEMM model of the yoke with an air gap and a permanent magnet. (b) FEMM model of the yoke with an air gap and a coil.

### 3.3 Yoke model with current carrying coil:

The last model that was used for evaluating the FEMM approach a similar yoke was used as shown previously. For this model the permanent magnet is replaced by a coil which generates a magnetic field when a current is put through this coil. For the yoke model with a coil a similar approach was used. Again Ampere's law, shown in equation 21, can be used to determine the magnetic field around a closed loop which can be related to the current passing through the loop, which in the case of a coil is the number of turns multiplied by the current through each wire. Since the equivalent circuit for a coil can be seen as a voltage source the reluctance of the yoke material is not neglected in this case [11]. If the air gap becomes zero this would result in a short circuit which would lead to an infinite current and therefor an infinite flux density. Since the yoke is surrounded by a medium which has a permeability this would mean the field is no longer contained inside the magnetic circuit and it will no longer be valid. Therefor the reluctance will be taken for steel. For the model with a coil Ampere's law gives the following:

$$\oint_C H d\ell = H_g g + H_\mathrm{C}(C-g) = \int_S J \cdot dS = N \cdot I \tag{26}$$

$$B_g = \mu_0 H_g = \mu_0 \left( \frac{N \cdot I}{g} - \frac{H_\mathrm{C}(C-g)}{g} \right) \tag{27}$$

The magnetic field inside the yoke material is dependant on the flux density and the relative permeability $\mu_r$ of the material, since the cross-sectional area is equal throughout the circuit we can assume that the flux density is constant thus we can compute the magnetic field inside the yoke as follows:

$$\mu_0 \mu_\mathrm{r} H_c = B_g \tag{28}$$

Substituting this into the previous equation gives the air gap flux density which can be used to compute the flux density as a function of the gap length.

$$B_g = \mu_0 \frac{N \cdot I}{\frac{1}{\mu_\mathrm{r}} C + (1 - \frac{1}{\mu_\mathrm{r}}) g} \tag{29}$$

The analytical expression will be used to calculate the flux density at different air gap lengths which can then be compared to the FEMM model shown in figure 3b.

### 3.4 Multimotor prototype design:

In order to compare finite element simulations to a motor setup, a first prototype of the BLDC multimotor was build. The control methods that will be tested on this motor will be discussed in the next section. For this design it was chosen to take the minimal amount of magnetic poles for the two individual rotors of this motor being 2 and 4 poles respectively. This was done to simplify the controllers required since the minimum number of coils needed is equal to the number of poles plus one extra coil. The reason for this is that the fields that need to be applied in the stator should have the same number of poles as the rotor that is being driven and it has to be placed with an offset of 90 degrees to achieve the maximum amount of torque. To be able to do this for any orientation of the rotors a minimum of 5 coils is needed in the case of a 4 pole rotor. Based on this the motor was designed with two rotors, one with 2 poles and one with 4 poles and a stator with 5 coils. The design also features two concentric axis to be able to lead the degrees of freedom out of the motor. The Solidworks model for this motor is shown in figure 4a as well as a picture of the final build of the motor which is shown in figure 4b. Labels are used to identify the different parts of the multimotor. The 2 pole rotor is mounted on output shaft 1 and the 4 pole rotor is mounted on output shaft 2, these will be referred to as outputs 1 and 2 respectively.

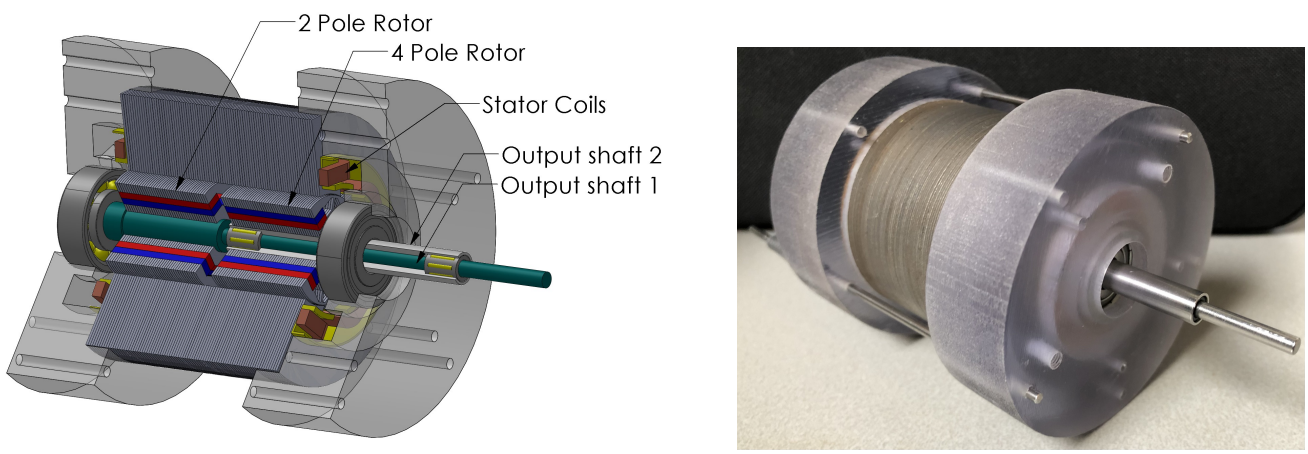


*(a)* *(b)*

Figure 4: The figure above shows the solidworks model (a) with labels indicating the different parts of the multimotor assembly and the prototype (b) that was built of the multimotor featuring two output shafts that was used for the measurements.

Based on the design of this motor a FEMM model was made which is shown in figure 5, in order to model the effect of the coil currents on the two rotors independently two seperate FEMM models will be used to compute the torque when currents are applied to the 5 coils of this motor. The assumption that is made here is that the field in the axial direction does not affect the rotors which is expected since the poles of the two rotors are always orthogonal to each other. Another reason why the axial flux leakage will be small is the fact that the motor was built using lamination's which aid in containing the field in the radial plane since the layers add more reluctance to the axial direction and there is a small bushing between the two rotors which adds a small axial gap between the two rotors. The two rotors are both made using 4 permanent magnets, the fact that one acts as a 2 pole rotor is achieved by aligning the two magnets on each side of the rotor. The 4 pole rotor is achieved by alternating the direction of the permanent magnets. In the results a figure will show how these two magnet orientations can achieve the correct number of magnetic poles in the two rotors.

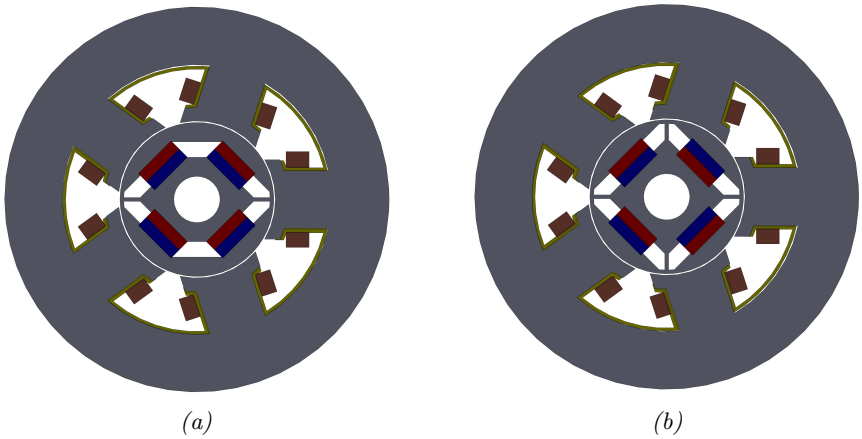


Figure 5: This figure shows the Solidworks models of the two separate rotors used for the prototype, the magnets and coils are shown in the same way as in the figure for the assembly. The rotor with 2 poles is shown in (a) and the rotor with 4 poles is shown in (b) these models can be converted to DXF format and directly imported into the FEMM program.

### 3.5 Experimental setup:

To compare the FEMM model to measurements that can be performed on the prototype that was built two different measurement setups were used. These setups were used to measure the static torque on the two output shafts and since FEMM only calculates static torque the dynamic torque was not measured. Another reason why dynamic measurements were not performed is due to the fact that the prototype had a few issues during the production phase. The main issue with the motor was the fact that the bearings were not properly aligned by the 3D printed parts that were used, this causes the rotor to touch the stator at certain positions and therefor is unable to rotate freely. This meant that the controllers described in the previous section could not be tested on the prototype and these will only be tested in FEMM.

The first measurement that was performed was by applying a known load to the two shafts of the motor. This load was applied using a lever and a few weights attached to the end of this lever, since the mass and length of the lever is know the torque required to lift this load can be computed. The current required to lift up the load was measured which results in the torque that the shaft experiences at that particular current. This same current can then be used in the FEMM calculation and the torque results can be compared which will be shown in the result section. This method was used to measure the torque on both output shafts and the setup is shown in figure 6.

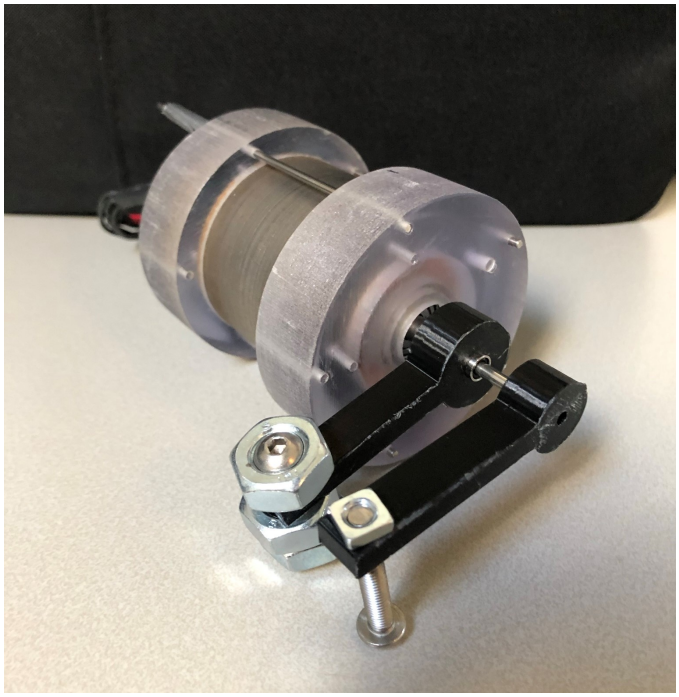

Figure 6: This figure shows the measurement setup that was used for the first static torque measurement where the current is measured at which the motor is able of lifting the weight, the torque is then computed since the length and mass of the lever are known.

The second torque measurement was performed using a scale. The same levers as in the previous setup are used here but instead of adding the weights the lever was used to push down on a scale resulting in a force measurement. This force measurement was then compared to the FEMM result by dividing the computed torque by the length of the lever. To make a good comparison the torque was computed in FEMM with taking into account a measurement error of $\pm 3°$ as well as a measurement error in the length of the lever which was $\pm 2$ mm due to fact that the contact point of the bolt with the scale has a diameter of 3 mm and an accuracy of 0.5 mm in measuring the length of the lever. With these measurement errors taken into account two lines will be plotted where the maximum and minimum torque will be plotted as a function of the current.

### 3.6 Control methods used for the multimotor:

Sinusoidal control and trapezoidal control will be compared in FEMM to see how well it can predict the performance difference that can be obtained in a multimotor and to show that the cross link torque is smaller than the nominal torque which would allow decoupling by applying a feedback controller. To properly define a control waveform that will be applied to the coils in the multimotor the first step was to determine what field needs to be created in the coils in order to achieve a positive torque on the two separate rotors. To do this a simplified setup was used for which a schematic is shown in figure 7.

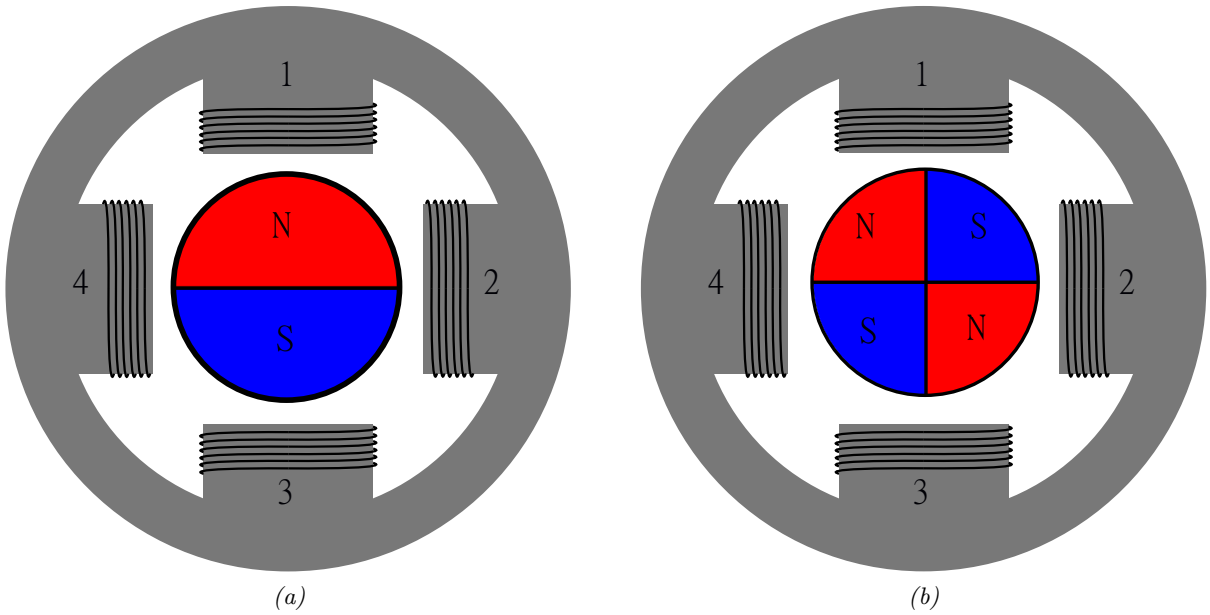


Figure 7: This figure shows a schematic of a simplified motor with 4 coils labeled 1 to 4 and two different rotors with 2 and 4 poles respectively (a) and (b).

In this example 4 coils are used which will act as a magnet with either a north or south pole when a positive or negative current is supplied through the coil. In the case of the 2 pole rotor coil 2 will be supplied with a positive current and coil 4 will be supplied with a negative current creating a north and south pole in the stator teeth. This way the rotor will experience a counter clockwise torque as it will align itself with the field created by the two coils due to the north pole being pulled to the south pole in the stator and the south pole being pulled to the north pole in the stator. The direction of the current can be reversed which reverses the direction of the torque. Once it rotates 90 degrees and aligns with this field it will no longer experience a torque. To ensure that a constant torque is experienced the field in the stator needs to be placed such that it has a relative angle of 90 degrees to the poles of the rotor. This same method can be applied to the 4 pole rotor shown in the same figure. This time all 4 coils can be used to generate a torque. This technique of switching the coils on or off and placing the field as close to 90 degrees as possible is called trapezoidal control [12]. A second method that will be tested is called sinusoidal or field oriented control. This technique applies the current as a sinusoidal waveform to the coils. This way the field in the stator rotates with the same period as the rotor ensuring that the field of the stator is always orthogonal to the rotor poles. Since this is not the case for the trapezoidal control it will suffer from a larger ripple in the torque.

In the multimotor the stator is shared between the two rotors, meaning that they are placed inside the same field that is generated by the stator. To see if the outputs are decoupled the cross link torque will be computed using the finite element method. This cross link torque is defined as the torque experienced by the 4 pole rotor while the waveform is applied that is meant to drive the 2 pole rotor and vice versa. In the case of the 4 coils shown in the schematic this cross link torque can be estimated directly. The first case would be driving the 2 pole rotor by applying a positive current to coil 2 and a negative current to coil 4. When looking at the 4 pole rotor and applying the same currents we see that the torque is not equal. The rotor experiences a counter clockwise torque due to the current through coil 2 since it acts as a north pole. The torque resulting from the negative current through coil 4 is counter clockwise since it acts as a south pole and it attracts the south pole of the rotor. The magnitude of the torque depends on

the current through the coils which is equal thus the total torque experienced by the rotor is zero as they are equal but in the opposite direction. This same approach can be used to show that the same applies for the field that would be used to drive the 4 pole rotor. This shows that for this position for the rotors in combination with 4 coils the expected cross link torque would be zero.
From figure 7 it can also be seen that if the 4 pole rotor rotates 45 degrees all poles align with one of the stator tooth. This is problematic as this means that the coils will not be able to generate a field in which the rotor experiences a torque, for this reason the prototype discussed previously has 5 coils. This makes sure that for any rotor position a field can be generated in which the rotor experiences a torque. The downside of using more coils is that the field generated using the previously described control methods will no longer result in two decoupled outputs. The fields will not be at exactly 90 degrees relative to the rotor poles and therefor the total torque will not cancel out entirely however it will still be smaller than the direct torque that is applied to the rotor for which the controller output is selected.
To test the control methods using FEMM the two control methods have to be defined for a motor with 5 coils. This was done for both the trapezoidal control as well as the sinusoidal control. The current waveforms for each method for the first coil is shown in figure 8. These waveforms will be applied to the remaining coils by adding a phase shift of 72 degrees which is the angle between the coils. The wave form for each coil resulting from this for driving the 2 pole rotor is shown in figure 9.

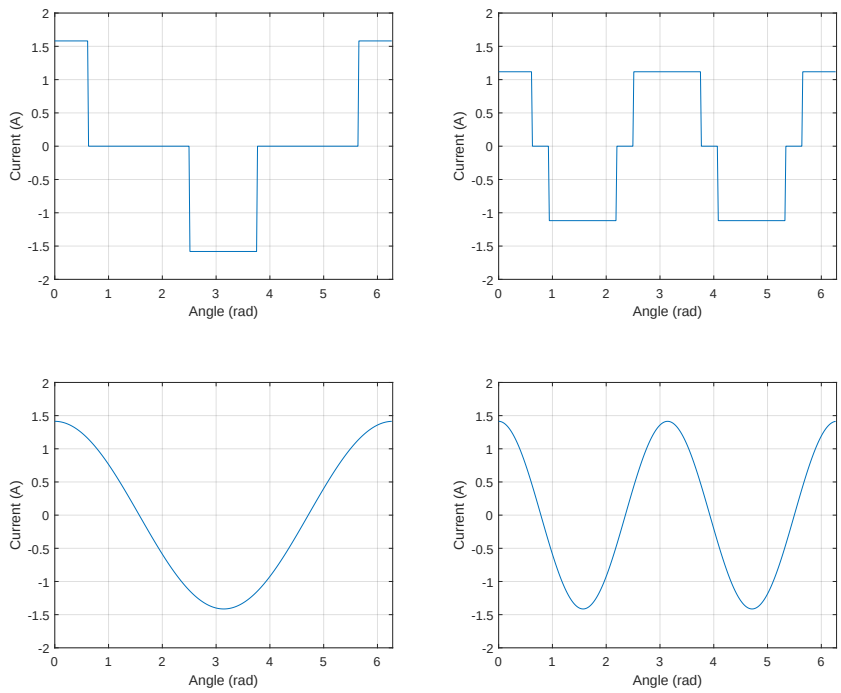


Figure 8: This figure shows the two different control techniques that will be simulated in FEMM. The left plots show the wave forms used for driving the 2 pole rotor shaft for both trapezoidal and sinusoidal respectively. The right plots show the wave forms used for driving the 4 pole rotor shaft.

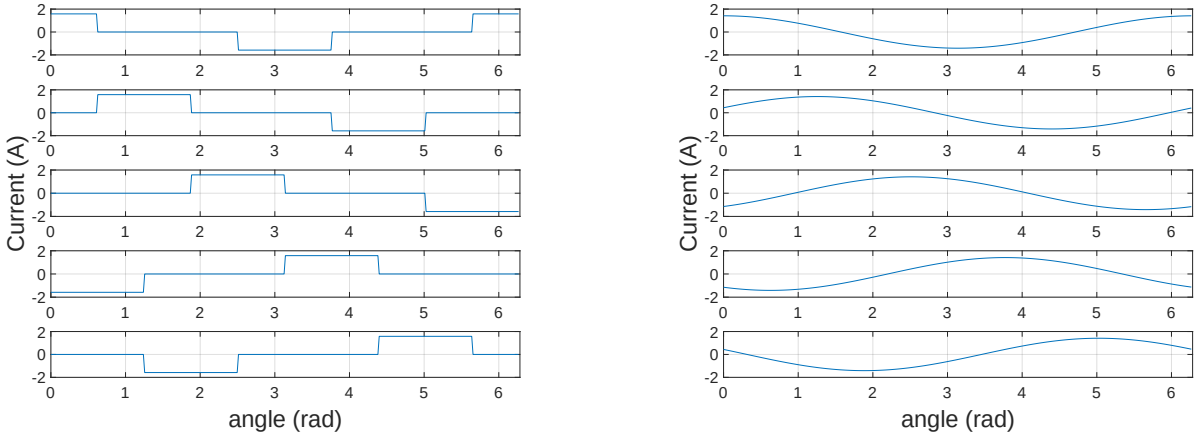


*(a)* *(b)*

Figure 9: This figure shows the current wave forms to drive the 2 pole rotor that will be used to simulate the torque output on the multimotor in FEMM. (a) shows the current wave forms applied to the 5 coils with respect to the angular position of the rotor using trapezoidal control, (b) shows the current wave forms applied to the 5 coils with respect to the angular position of the rotor using sinusoidal control

# 4 Results and discussion

## 4.1 Dipole model:

To validate the dipole field in FEMM a small magnet was used of which the field will be measured at a distance, this is needed for the dipole model to accurately describe the field of a magnetic source that is not a perfect dipole. The FEMM results are compared to the dipole model that was derived in section 3.1. The results are also compared to a planar approach. In this approach the magnet is modelled as two surface currents on the sides of the permanent magnet, this way the field can be calculated as a superposition of the field representation of two infinitely long wires. The results of the two approaches as well as the FEMM calculation are shown in figure 10.

Looking at the results for this dipole approach we can see clearly that the 3D representation of the dipole does not match the FEMM calculation. The second approach using the planar approximation of an infinitely long bar magnet shows better results. The order with which the flux density decreases over distance matches the FEMM calculation. The remaining difference between the FEMM calculation and the analytical model is larger for small distances with a peak of 10 %. At larger distances the error reduces significantly. The mean value of the difference between the analytical model and the FEMM calculation is 1.12 %. Besides the offset between the two curves some periodic variations can be seen in the FEMM calculations, which are not present in the analytical results.

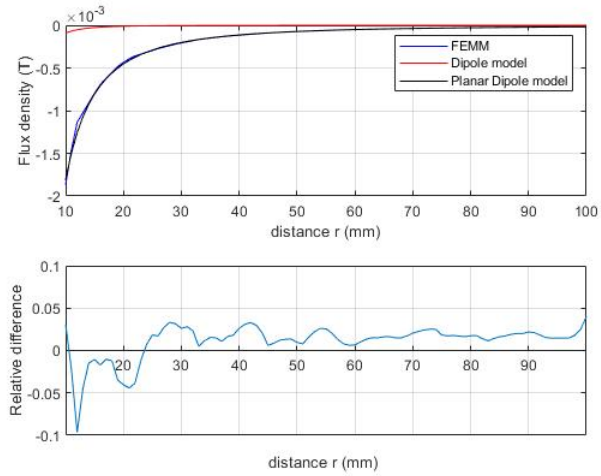


Figure 10: The first plot in this figure shows the flux density as a function of the distance at which the field is measured for the dipole model, the analytical model of an infinite bar magnet and the FEMM model for a permanent magnet. The second plot shows the relative difference between the analytical model of the infinite bar magnet and the FEMM result.

### 4.2 Yoke model with permanent magnet:

The second model that was analyzed is the yoke model with a permanent magnet. To calculate the air gap flux density analytically a lumped element model was used as described previously. This model was compare to the FEMM model in which the same material properties were used for the permanent magnet. The yoke permeability is neglected in this model since it only has a very small effect on the model. The major reluctance in the lumped model that we are interested in is the air gap reluctance. The results are shown in 11, from this plot we can observe the following. Firstly we can clearly see that the difference when no air gap is present is very close to 0. This result was expected as this is the situation in which the north and south pole of the magnet are connected by a medium which no reluctance. In terms of the lumped element model this can be seen as a short circuit of a current source, which results in an equal current in the conductor that has no resistance. When the air gap increases the difference increases as well, this difference between the model and FEMM can be expected as the lumped model assumes an equal distribution of the flux over the air gap and does not take any stray fields into account. These stray fields occur around the edges of the air gap and effectively increase the area over which the flux inside the circuit is distributed. This could be approximated to further improve the accuracy of the model [11] by taking into account the ratio between the width and height of the gap. This explains why the FEMM result gives lower values for the air gap flux density compared to the analytical model.

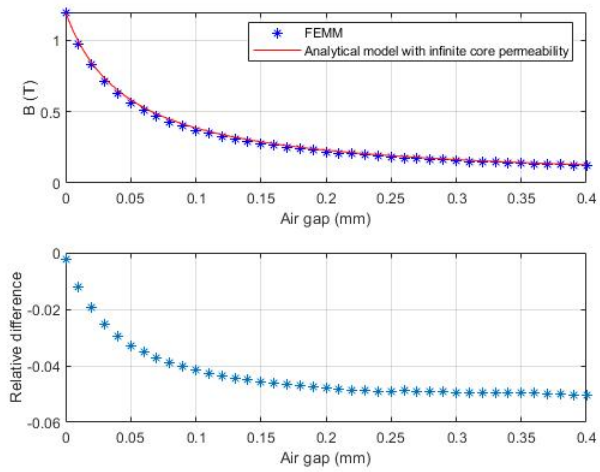


Figure 11: The first plot in this figure shows the air gap flux density as a function of the air gap length for both the FEMM model shown in figure 3a and the analytical model for the yoke with a permanent magnet that was described in the method. The second plot shows the relative difference between the FEMM model and the analytical model as a function of the air gap.

### 4.3 Yoke model with current carrying coil:

The third analytical model that was analyzed is the yoke model with a coil. The yoke has the same dimensions as the yoke model shown in the previous section. The coil has 10 turns carrying 1A. For this model Ampere's law was used to determined the H field on a closed contour which is equal to the total current passing through the surface inside the contour. Using this model the results are shown in figure 12. Comparing it to the calculated results in FEMM it can be seen that the difference behaves similarly to that of the yoke model with permanent magnet. Since the yoke reluctance was not neglected in this model the flux density with no air gap is larger, this is due to the non linearity of the permeability of the material that was used. The field for small air gaps exceeds 1 T, at this point the permeability of the steel will decrease as it starts to saturate. This results in a higher yoke reluctance and therefor a reduced flux density. The yoke reluctance was not neglected in this model as a coil in an equivalent magnetic circuit acts as a voltage source, which means it would short the voltage source if the yoke reluctance is neglected and the flux density would rise to very high values. At this point the non linear behaviour of the yoke can no longer be neglected and it would result in an incorrect analytical model.

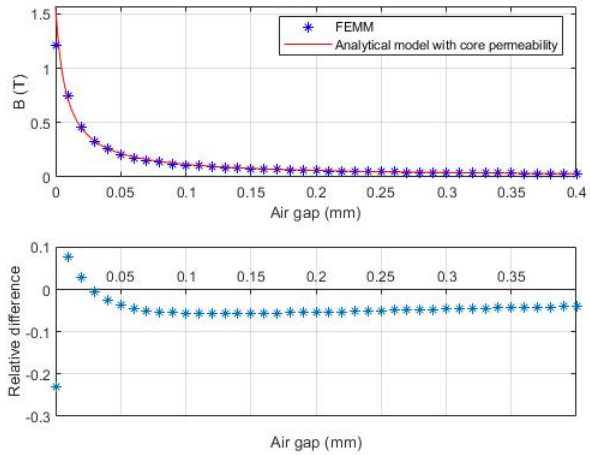


Figure 12: The first plot in this figure shows the air gap flux density as a function of the air gap length for both the FEMM model shown in figure 3b and the analytical model for the yoke with a coil that was described in the method. The second plot shows the relative difference between the FEMM model and the analytical model as a function of the air gap.

### 4.4 Measurement results:

To compare the measurement results to the FEMM model the previously shown Solidworks models were imported into FEMM. The first step was to verify that the rotor fields indeed show a field that matches the number of magnetic poles in the design. The fields that are obtained from the FEMM model are shown in figure 13 and it matches the expectations. The 2 pole rotor can be recognized by the two closed loops of flux lines and the 4 pole rotor can be recognized by the 4 closed loops of flux around. Another observation that can be made from this is that flux density in the rotor core is very high which means that the material is partially saturated.

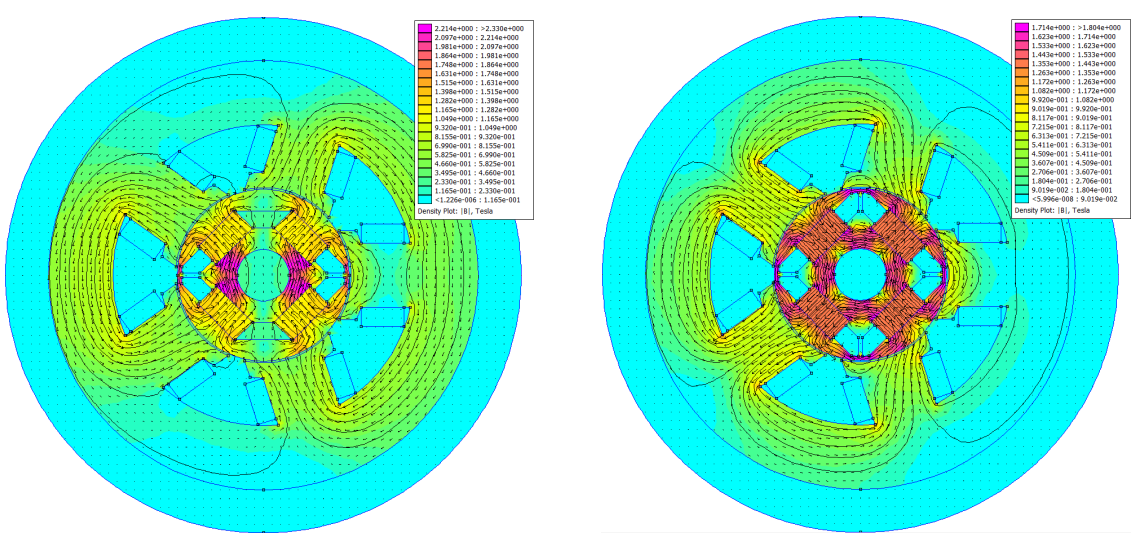

*(a)* *(b)*

Figure 13

The measurement that were performed using the first measurement setup where weights are applied to the motor using a lever are shown in figure 14. From these measurements it was seen that the results match well with the torque that was computed using the FEMM model. The measurements show a linear relationship to the current as expected where the data points at higher currents seem to deviate from this line. This could be caused by the fact that at higher currents the field generated by the coil could cause the yoke material to become saturated, as was observed in the yoke model with a coil in which the yoke permeability was taken into account.

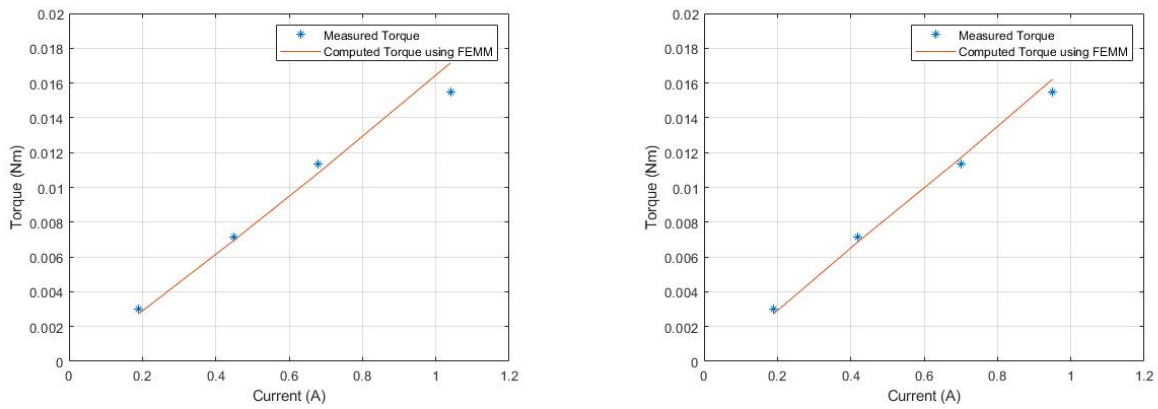


*(a)* *(b)*

Figure 14: The two figures above show the static torque measurement with the method of applying a known load to the shaft and measuring the current at which the torque drops, these torque measurements are shown for the 2 pole shaft (a) and the 4 pole shaft (b) as well as the computed torque using the FEMM models as described in the method.

The second measurement that was performed which was done using a scale is shown in figure 15. In this figure the two possible measurement errors are taken into account. These measurements errors include the length of the arm at which the force was measured as well as the possible error in the rotor angle. This is indicated by the two lines which are obtained using the FEMM model. From this figure it can be seen that the data points are within the region bounded by these two lines, however the gradient of this line seems to be higher than the gradient of either of these two lines. This indicates that the relation between current and torque is different in the measurements than in the FEMM model. There are a number of possibilities which could cause such a deviation from the model. These include the number of turns in the motor as they are manually applied an error could have been made resulting in a larger amount of turns. Secondly the air gap in the multimotor could be smaller due to the misalignment of the shaft. This was observed during the measurments since the rotor touches that stator at parts of the rotation in which case the air gap would be zero. This could also be caused by the bending of the shaft under large radial loads. Lastly a possible factor that could cause a difference between the measurements and the FEMM simulations would be the fact that the stator part of the motor is longer than the actual rotors. This would mean that the stator has an overhang relative to the rotor. Part of the stator around the edge of the rotor would still contribute to the field inside the rotor and thus the actual rotor length would be slightly longer. If this would be applied in the FEMM simulation this could also result in a slightly higher torque at a given current.

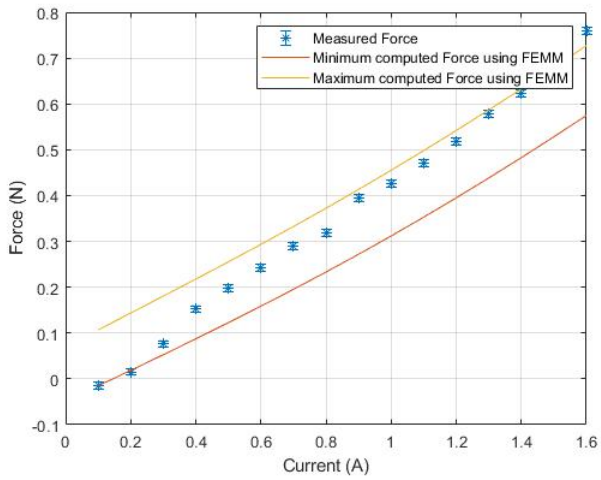


Figure 15: This figure shows the static force measurement using a lever which pushes on a scale for the 2 pole rotor shaft, the force is plotted as a function of the current applied and the results of the FEMM model is shown in the same graph. For the FEMM model two calculations are performed taking into account the measurement error in the angle and length of the lever.

### 4.5 Testing control methods in FEMM:

The control techniques that will be tested to see how their performance compares are sinusoidal and trapezoidal control which were discussed in section 3.6. The results obtained when applying these control techniques will be tested on three different performance measures. The nominal torque, torque ripple and the cross link torque will be computed in FEMM such that they can be compared for each rotor. This gives an insight in which control method gives the most performance for the multimotor. The first results that were computed are the nominal torque and torque ripple which is shown in figure 16.

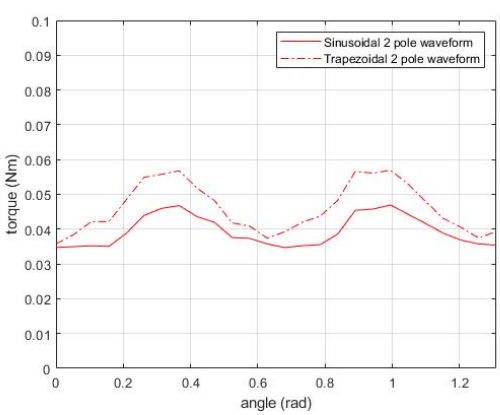


*(a)* Nominal torque output on the 2 pole rotor shaft when applying the 2 pole current waveform.

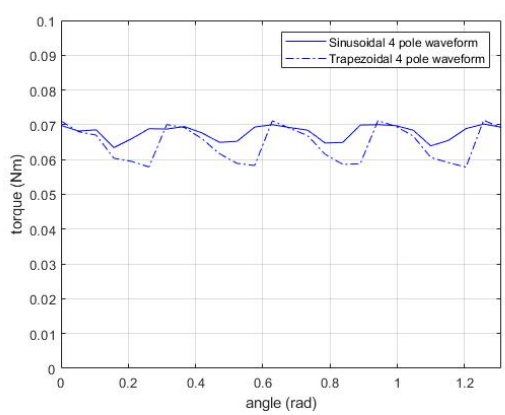


*(b)* Nominal torque output on the 4 pole rotor shaft when applying the 4 pole current waveform.

Figure 16: The two figures above show the nominal torque output on the two separate output shafts. Red indicates the 2 pole rotor shaft, blue indicates the 4 pole rotor shaft, trapezoidal control is indicated by the dashed line and sinusoidal control is indicated by the continuous line.

Looking at these results we can see that the torque ripple, which is measured by taking the amplitude, is reduced when comparing trapezoidal to sinusoidal control on both output shafts. In the case of the 2 pole output shaft in figure 16a the amplitude of the torque ripple reduces from 0.0212 N m to 0.0123 N m when comparing trapezoidal to sinusoidal control, which is a reduction of 41.9 %. In the case of the 4 pole output shaft in figure 16b the amplitude of the torque ripple reduces from 0.0135 N m to 0.0068 N m when comparing trapezoidal to sinusoidal control, which is a reduction of 49.6 %. This is in line with the expectations as sinusoidal control is placing the field in the stator at a constant angle relative to the rotor position. Besides the reduction in torque ripple it can also be seen that the nominal torque is not equal for the two separate output shafts. The nominal torque is computed by taking the mean value of the torque outputs shown in the figure above. The nominal torque on the 2 pole output shaft is 0.0469 N m and the nominal torque on the 4 pole output shaft is 0.0641 N m, both using trapezoidal control. This difference is relatively large, the reason this happens could be due to the fact that the current waveform that is used to generate the nominal torque on the 4 pole shaft has 4 coils which are supplied with a high current whereas the current waveform used to drive the 2 pole shaft only has 2 coils that are close to a maximum. This can be solved by scaling the current waveforms such that they generate an equal nominal torque rather than scaling them to have an equal RMS value.
The second calculation that was performed was to compute the cross link torque. This is the torque experienced by one of the output shafts while the control input is given that generates the nominal torque on the other output shaft. This result is shown in figure 17. From this figure we can see clearly that the cross link torque has a mean value which is close to zero.

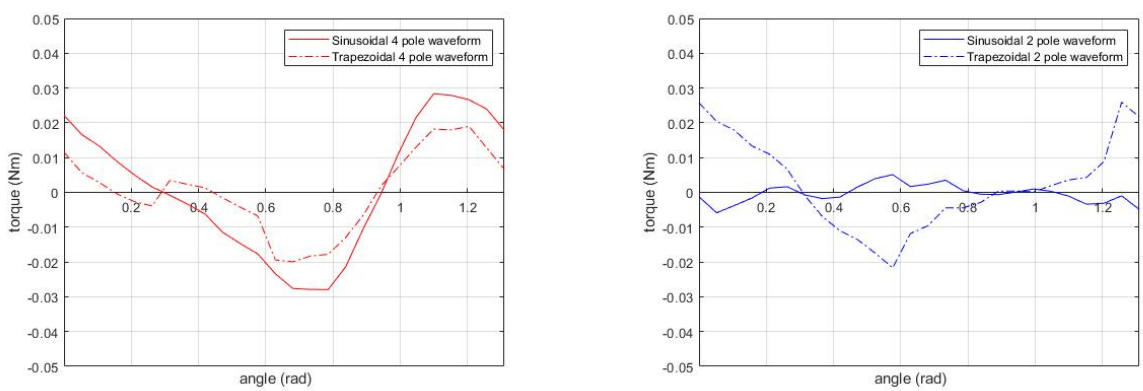


*(a)* Cross link torque output on the 2 pole rotor shaft when applying the 4 pole current waveform.

*(b)* Cross link torque output on the 4 pole rotor shaft when applying the 2 pole current waveform.

Figure 17: The two figures above show the cross link torque output on the two separate output shafts. Red indicates the 2 pole rotor shaft, blue indicates the 4 pole rotor shaft, trapezoidal control is indicated by the dashed line and sinusoidal control is indicated by the continuous line.

For the 2 pole rotor shown in (a) this mean value is $-1.019 \times 10^{-4}$ N m and $-1.462 \times 10^{-4}$ N m for sinusoidal and trapezoidal control respectively. For the 4 pole rotor shown in (b) the mean value of the cross link torque is $1.0749 \times 10^{-5}$ N m and $5.6075 \times 10^{-4}$ N m for sinusoidal and trapezoidal control respectively. This result shows that in the case where either of the output shafts is driven by the nominal torque the other shaft will experience a torque, however over a full rotation the amount of work that is performed on this shaft is small compared to the nominal torque for both control methods.
The second observation that can be made from this graph is that in the case of the 2 pole rotor the cross

link torque for both control methods is relatively large, being 0.0286 N m and 0.0195 N m. This cross link torque could cause oscillations as it switches direction halfway through a rotation. In the case of the 4 pole rotor it can be seen clearly that the sinusoidal control significantly reduces the maximum value of the cross link torque. For the 4 pole rotor the maximum cross link torque values are 0.0056 N m and 0.0260 N m for sinusoidal and trapezoidal control respectively. A possible reason for the fact that the cross link torque on the 2 pole shaft is significantly higher is that it suffers more from the unbalanced field in the stator. The stator has 5 coils which means the field will not be symmetric. This could be improved by using an even number of coils as this would have opposing coils that cancel each other out as was discussed in the method. The 4 pole rotor since it uses more coils to generate the desired field could suffer less from this. This should be tested further to optimize the design and reduce the cross link torque on the output shafts as this would decouple the two output shafts better.

### 4.6 Discussion:

Looking at the results obtained we can see that the FEMM model verification using analytical results showed a good match between the models and the FEMM simulation for the planar dipole model. The two yoke models however show a larger error, this error goes up to 5 % for an air gap of 0.4 mm in the case of both models, this could be explained by the fact that the analytical model assumes an even distribution of flux inside the air gap and it neglects any flux that would pass outside the area directly between the two surfaces of the yoke. This spreading of field is usually referred to as a stray field, to verify if the difference between FEMM and the analytical model is caused by this an identification of the leakage reluctance will have to be performed which can be used to approximate the amount of flux leaking through different paths other than the air gap. This way the flux density in the air gap can be computed more accurately. Since the final results shown for the control methods give an improvement which is much greater than the aforementioned 5 % deviation from the model it was decided that this difference is sufficiently small. The fact that the yoke model with a coil has a much larger error when the air gap closes entirely can only be accounted for if the non linearity in the permeability of the yoke material is taken into account. Simply taking the yoke permeability as infinite would result in an infinite amount of flux density which is not possible to model with FEMM therefor it will always show a deviation from the analytical model. Since the final motor has an air gap it would not suffer from this as well as the fact that the motor parts were chosen with sufficiently large dimensions to ensure the amount of saturation occurring would be minimal.

# 5 Conclusion

In this report a first approach towards testing and validating a BLDC multimotor was presented. This motor has two concentric output shafts which by defining a proper control method can be individually driven. The validation was performed using a planar finite element analysis in FEMM. The first step was to validate the planar finite element method by comparing to models that can be computed analytically. These models include a dipole model, a yoke model with a permanent magnet and a yoke model with a coil. With this approach it was found that the analytical models match the FEMM models with an accuracy of 5 % when an air gap of 0.4 mm is used. The relative difference between the dipole model and the FEMM simulation was 1.12 %. From this it can be concluded that the accuracy with which FEMM is capable of determining the field in a magnetic circuit is 5 %, further analysis of the yoke models could reduce this accuracy as the flux leakage outside of the yoke is not taken into account in the analytical models. The second method that was applied to verify the FEMM simulations was performed using a prototype multimotor. The prototype motor that was built features two concentric shafts with a shared stator and the motor was also modelled in FEMM. Two different measurement techniques were used to measure the static torque, the first being a measurement with a load applied to the output shaft and measuring the current through a single coil at which the motor was able to deliver the torque required to lift up the load. The second measurement was taken by pushing down on a scale using a lever which was mounted on the output shafts of the motor. These two measurement techniques were compared to the FEMM simulations in which measurement errors were taken into account including the angle at which the measurement was taken as well as the length of the lever which was used to convert the force to torque. These results matched within the modelled values from the FEMM model.

From these two methods we can conclude that FEMM is capable of modelling the torque output on the multimotor well and the accuracy with which it can compute the field strength within a magnetic circuit is 5 %. Given that the FEMM model was verified this model can be used to compare the outputs when the control methods are applied which are needed to achieve two decoupled outputs. The control methods that were compared are sinusoidal and trapezoidal control. These two control methods were applied to the two separate motor shafts to compute the nominal torque output they give as well as the cross link torque that they experience as a result of driving the other output shaft with the nominal torque. The comparison between the sinusoidal control and trapezoidal control matched the expectation in the sense that it greatly reduced the torque ripple. Applying sinusoidal control in stead trapezoidal control resulted in a reduction in ripple torque of 41.9 % and 49.6 % for the two output shafts respectively. The second performance parameter that was calculated using the FEMM model was the cross link torque for which the amplitude as well as the mean value was important. For this it was also expected that sinusoidal control would reduce the maximum cross link torque, however this was only the case for the output shaft with 4 poles on the rotor. The mean value of the cross link torque for both output shafts was negligible when compared to the nominal torque output that they can deliver. This means that based on the simulation result we can say that a decoupled motor with two output shafts is achievable as they are capable of delivering a constant output torque. The torque experienced as a result of driving the other output shaft might result in oscillations but they will not perform any work on the output as the integral of torque over a full rotation is negligible. This leads to the final conclusion which answers the research question as stated in the introduction: How accurately can different control methods be validated and tested using a planar finite element model for BLDC multimotors?

The planar finite element model is capable of computing the magnetic field inside a magnetic circuit with an accuracy of up to 5 %. Based on the validated FEMM model the control methods for realizing independent degrees of freedom on a multimotor were tested and showed that it is possible to obtain two decoupled degrees of freedom with this motor setup. The results have shown that sinusoidal control has improved performance over trapezoidal control as it reduces the torque ripple by at least 41.9 % for both outputs.

Further improvements can be made by testing if balancing the fields reduces the torque ripple as well as possible oscillation due to the cross link torque and a new prototype with higher tolerances needs to be made to verify the dynamic behaviour of the multimotor.

### Future Recommendations:

Since the results that were shown for the comparison of control methods were only using the planar finite element approach as the prototype suffered from some issues during the implementation some recommendations can be made. The first being the fact that the radial loads on the shaft were more significant than expected, under this load the motor shaft bends which results in the rotor to touch the stator surface. This causes the motor to get stuck which meant it was not possible to measure torque over a full rotation of the motor but only on parts off the rotation where it was still able to move freely under load. This can be improved by increasing the shaft stiffness or reducing the radial load. The first can be achieved by using a different material or using a larger diameter shaft. The latter might be possible by investigating the radial loads more thoroughly and perhaps a different number of stator coils and rotor poles will result in a more balanced field thus reducing the radial loads the rotor experiences. Apart from the stiffness that was found to be an issue another issue that was observed was in the misalignment of the shafts, this was caused by the inaccuracy of the 3d printed parts that were used which seated the bearings. Machined parts should be used for this such that a much higher accuracy can be achieved. This has the added benefit of potentially reducing the air gap.

Apart from the mechanical improvements to the motor another important part of the motor is the sensor that reads the angle of the shafts. This is required as a BLDC motor is a closed loop system and for the proper control to be applied the angle needs to be measured. A setup was made using encoders, which has not been tested since the motor was unable to freely rotate. This setup can be used if the number of output shafts is 2 at most. More output shafts would mean at least one of them is physically impossible to mount an encoder to unless it is placed next to the rotor or on the output shaft which is not a suitable placement. For testing purposes this can be used but for proper operation of the multi-motor a different solution should be found. A possibility for this would be to use the back EMF which is induced in the coils. This needs to be worked out into more detail to determine if it is possible to identify the two rotor positions from the combined back EMF of the two rotors. In order to properly do this a dynamic analysis of the motor needs to be performed which has not been done in this report.

These factors should be taken into account in the next step towards a fully functional multi-motor which can be taken into account in a design phase where the motor is optimized. The design parameters that can be taken into account in this case would be the dimensions of both the rotor and stator as well as their geometries, the number of coils in the stator as well as the number of poles on the rotors, the number of windings for each coil, the mechanical design of the concentric shafts and lastly the sensor assembly.

## Acronyms

**BLDC** Brushless Direct Current. 3–5, 11, 24, 25

**DOF** degree of freedom. 5, 6

**FEMM** Finite Element Method Magnetics. 3, 7–13, 15–21, 23, 24

## References


[1] D. Uygun, S. Solmaz, A. Turan, and S. Ruzgar, "A new topology for dual rotor/stator bldc motors applied to marine thrusters," vol. 2015, pp. 353–359, 09 2015.

[2] P. Bolognesi, O. Bruno, A. Landi, L. Sani, and L. Taponecco, "Electromagnetic actuators featuring multiple degrees of freedom: a survey," 09 2004.

[3] J. Ahn, S. C. Go, S. Kim, J. Lee, and H. Kim, "A study on digital control of 3-d.o.f. bldcm using labview," in *INTELEC 2009 - 31st International Telecommunications Energy Conference*, 2009, pp. 1–4.

[4] I. Boldea, L. Tutelea, S. Deaconu, and F. Marignetti, "Dual rotor single- stator axial air gap pmsm motor/generator drive for hevs: A review of comprehensive modeling and performance characterization," 10 2012, pp. 1–8.

[5] L. Xu, M. Lin, X. Fu, X. Zhu, C. Zhang, and W. Wu, "Orthogonal magnetic field analysis of a double-stator linear-rotary permanent magnet motor with orthogonally arrayed permanent magnets," *IEEE Transactions on Magnetics*, vol. 53, no. 11, pp. 1–4, 2017.

[6] D. J. Griffiths, *Introduction to electrodynamics; 4th ed.* Boston, MA: Pearson, 2013, re-published by Cambridge University Press in 2017. [Online]. Available: https://cds.cern.ch/record/1492149

[7] T. L. Chow, *Introduction to electromagnetic theory: a modern perspective.* Jones & Bartlett Learning, 2006.

[8] R. Zhou, G. Li, Q. Wang, J. He, and T. Wang, "Drive current calculation and analysis of permanent magnet spherical motor based on torque analytical model and particle swarm optimization," *IEEE Access*, vol. PP, pp. 1–1, 03 2020.

[9] S. Ye and X. Yao, "Fast analytical calculation of the air-gap flux density in an outer-rotor permanent-magnet brushless motor," *MATEC Web of Conferences*, vol. 189, p. 06008, 01 2018.

[10] S. K. L. V. and N. K. G. V., "Power conversion in renewable energy systems: A review advances in wind and pv system," *International Journal of Energy Research*, vol. 41, no. 2, pp. 182–197, 2017. [Online]. Available: https://onlinelibrary.wiley.com/doi/abs/10.1002/er.3601

[11] S. Barmada, R. Rizzo, and L. Sani, "Didactic considerations on magnetic circuits excited by permanent magnets," *Education, IEEE Transactions on*, vol. 52, pp. 532 – 537, 12 2009.

[12] B. Akin and M. Bhardwaj, "Trapezoidal control of bldc motors using hall effect sensors," *Texas instruments*, 2010.